ACS OMEGA

http://pubs.acs.org/journal/acsodf

Article

Biochar Derived from Chinese Herb Medicine Residues for Rhodamine B Dye Adsorption

Pengwei Li, Ting Zhao, Ziheng Zhao, Hanxiao Tang, Weisheng Feng, and Zhijuan Zhang*

Cite This: *ACS Omega* 2023, 8, 4813−4825

Read Online

ACCESS | Metrics & More | Article Recommendations | Supporting Information

ABSTRACT: In this study, one well-known CHM residue (*Atropa belladonna* L., ABL) was used to prepare biochar capable of adsorbing rhodamine B (RhB) with an ultrahigh surface area for the first time. Three micropore-rich ABL biochars including ABL@$ZnCl_2$ (1866 m^2/g), ABL@H_3PO_4 (1488 m^2/g), and ABL@KOH (590 m^2/g) were obtained using the one-step carbonization method with activation agents ($ZnCl_2$, H_3PO_4, and KOH) via chemical activation and carbonization at 500 °C, and their adsorption performance for RhB was systematically studied with adsorption kinetics, isotherms, and thermodynamics. Through pore diffusion, $\pi-\pi$ interaction, and hydrogen bonding, ABL biochar had excellent adsorption performance for RhB. Moreover, when C_0 was 200 mg/L, biochar dosage was 1 g/L, and the contact time was 120 min; the maximum RhB adsorption capacity and removal efficiency on ABL@$ZnCl_2$ and ABL@H_3PO_4 were 190.63 mg/g, 95% and 184.70 mg/g, 92%, respectively, indicating that it was feasible to prepare biochar from the ABL residue for RhB adsorption. The theoretical maximum adsorption capacities of ABL@$ZnCl_2$ and ABL@H_3PO_4 for RhB were 263.19 mg/g and 309.11 mg/g at 25 °C, respectively. Furthermore, the prepared biochar showed good economic applicability, with pay back of USD 972/t (ABL@$ZnCl_2$) and USD 987/t (ABL@H_3PO_4), respectively. More importantly, even after five cycles, ABL@H_3PO_4 biochar still showed great RhB removal efficiency, suggesting that it had a good application prospect and provided a new method for the resource utilization of traditional CHM residues. Additionally, pore diffusion, $\pi-\pi$ interactions, and hydrogen bonding all play roles in the physical adsorption of RhB on ABL biochar. $\pi-\pi$ interactions dominated in the early stage of RhB adsorption on ABL@H_3PO_4, while pore diffusion played a crucial role in the whole adsorption process on both adsorbents.

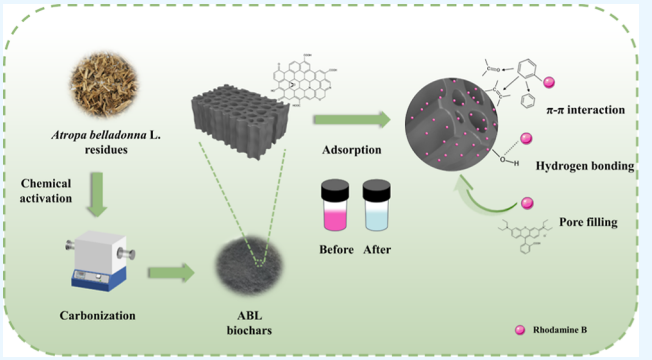

1. INTRODUCTION

Dyes, divided into three categories: anionic, cationic, and nonionic dyes,[1] which are widely used in the textile,[2,3] printing, papermaking, leather, and cosmetic industries, have been classified as the highest-priority water pollutants.[4,5] Nevertheless, the poor degradability of organic dyes upon radiation and oxidation makes them difficult to eliminate.[6] Once these substances are discharged into water bodies, their persistence prevents the penetration of sunlight to the deepest levels and changes the photosynthetic activity of the aquatic environment.[7−9] Additionally, they increase the turbidity of wastewater that leads to the deterioration of water quality.[10,11] Rhodamine B (RhB) is an extensively used synthetic anthraquinone cationic dye, which is reported to be highly toxic and carcinogenic, causing detrimental effects, for instance, cognitive impairment, anemia, kidney damage, and reproductive toxicity.[12,13] Moreover, the extensive use of RhB is noxious when inhaled and ingested, leading to liver and thyroid damage and eye and skin irritation. Therefore, there is an urgent need to remove harmful dyes from wastewater.

Currently, a number of techniques have been employed to effectively remove RhB from contaminated wastewater, including sedimentation, chemical flocculation[9] and coagulation, ion exchange, photocatalysis,[14,15] and membrane separation.[16,17] However, these techniques have several drawbacks, such as toxic by-products, high energy consumption, odor production, and the requirement of a large treatment area. Except for these techniques, adsorption is regarded as an effective, reliable, affordable, and sustainable approach for organic dye removal from wastewater owing to its industrial-scale applicability and high efficiency.[18] Adsorbents such as zeolites,[19,20] metal−organic frameworks (MOFs),[21] biochar,[22] and nanotubes[23,24] have been widely studied for dye removal. Because of its wide range of raw materials, feasibility of industrialization, a simple preparation process, and low cost, biochar has become the most promising adsorbent.[25] Consid-

Received: October 29, 2022
Accepted: January 18, 2023
Published: January 27, 2023

https://doi.org/10.1021/acsomega.2c06968
ACS Omega 2023, 8, 4813−4825

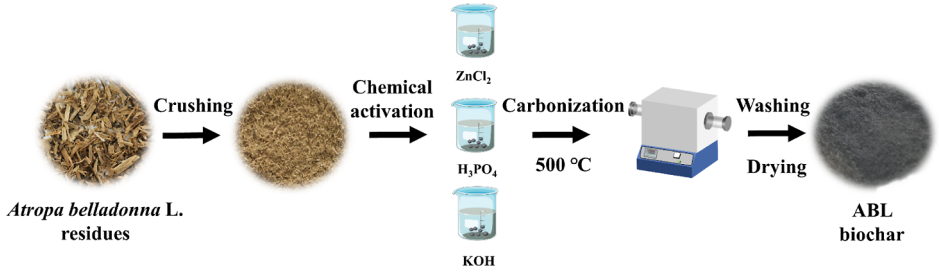

Figure 1. Flow chart of ABL biochar preparation.

ering the increasingly prominent energy crisis and the consideration of lower cost, numerous waste biomasses, such as poultry manure,[26] sludge,[27] crop waste,[28] peel,[29] and waste,[30] have been studied for the preparation of biochar for various applications.

Chinese herb medicine (CHM) is a treasure of the Chinese nation that has made great contributions to human health. With the development of CHM, many CHM residues have emerged.[31] In China, it is recorded that approximately 70 million tons of CHM residues are generated each year in China,[32] and CHM residues are becoming one of the largest biomass resources at present. Nevertheless, most CHM residues are poorly reused, leading to a giant waste of resources. Nowadays, extensive techniques have been adopted to treat waste resources, especially CHM residues, such as stacking, landfilling, or incineration, all of which result in heavy environmental pollution and resource wastage.[33] Therefore, it is necessary to develop these resources into economical, environment-friendly, and usable materials to mitigate environmental pollution and achieve the sustainable effect of "treating waste with waste". It is well known that CHM residues are abundant in cellulose, hemicellulose, lignin, and various microelements as well, for example, iron, calcium, and phosphorus.[34] Furthermore, the affluent functional groups and open stomata of CHM residues can help in preparing biochar for efficiently capturing dyes in aqueous solutions.[35] Vigneshwaran et al.[36] developed a sulfur-doped tapioca peel biochar with a specific BET surface area of 146 m^2/g, while its RhB adsorption capacity was 33.10 mg/g at 298 K. Mousavi et al.[11] recorded a maximum RhB adsorption capacity of 5.6 mg/g on biochar derived from corn stalks. Although these biomass/residues show good potential for dye treatment, their poor dye adsorption capacities and small surface areas are major obstacles. Consequently, it is requisite to select appropriate CHM raw materials to prepare biochar with a high surface area and good RhB adsorption performance to achieve efficient removal.

Herein, a kind of well-known CHM named *Atropa belladonna* L. (ABL) was chosen to study the application of CHM residue in wastewater treatment. To our knowledge, there is no report on the preparation of biochar from ABL residue and its application in wastewater treatment. Thereafter, the micropore-rich ABL biochar was prepared from waste ABL via chemical activation and carbonization for the first time, and its adsorption performance for RhB was systematically studied with adsorption kinetics, isotherms, and thermodynamics. The structural properties of the ABL biochar were characterized. Then, the effects of adsorbent dosage, initial dye concentration, contact time, pH, and adsorption kinetics, as well as the isotherm of RhB adsorption on ABL biochar, were investigated. Moreover, the potential adsorption mechanism of RhB on ABL biochar was deeply discussed. The industrial and economic feasibility of ABL biochar was well evaluated. The performance of CHM-derived biochar for RhB adsorption was thus investigated systematically in this work.

2. MATERIALS AND METHODS

2.1. Chemicals and Materials. The CHM residues (*A. belladonna* L., ABL) were acquired from a Chinese medicine factory in Henan, China. The activation ingredients, that is, zinc chloride ($ZnCl_2$), phosphoric acid (H_3PO_4, 85%), and potassium hydroxide (KOH) were bought from Shanghai Macklin Biochemical Co., Ltd. RhB was purchased from Shanghai Aladdin Biochemical Technology Co., Ltd. Commercial biochar was purchased from a biochar factory in Henan, China. All chemicals were used as received without further treatment.

2.2. Preparation of ABL Biochar. Figure 1 depicts the preparation flow chart of the as-synthesized ABL biochar. First, ABL residues were thoroughly rinsed with distilled water, air-dried for 2 days, and pulverized to obtain a uniform particle size of 100−150 mesh before conducting the experimental steps to prepare biochar. Subsequently, the cleaned ABL residues (2 g) were immersed separately in 2 M $ZnCl_2$, 3.6 M H_3PO_4, and 5 M KOH solutions for 24 h and then dried in an oven at 80 °C for 12 h. The mixture was pyrolyzed at 500 °C under a N_2 flow for 2 h in a tube furnace with a heating rate of 5 °C/min. The details of experimental parameters selected are shown in the Supporting Information (Tables S1−S4). After activation, the as-made ABL biochar was washed with 5% HCl followed by distilled water until a neutral pH value was reached prior to drying at 80 °C in an oven for 12 h. The samples activated by different chemical reagents were labeled ABL@x (x = $ZnCl_2$, H_3PO_4, and KOH, respectively). However, the sample carbonized directly without chemical reagents was labeled ABL@Blank.

2.3. Characterization. The ash content and moisture content of raw ABL residue were tested as reported.[37] The pore structures were measured by N_2 adsorption−desorption isotherms at 77 K using an automated sorption analyzer (Autosorb IQ_2, Quantachrome). The element composition was investigated by an elemental analyzer (EA, Elementar UNICUBE). The surface morphology and chemical composition of biochar samples were observed by scanning electronic microscopy (SEM, Zeiss Evo 18) coupled with energy dispersive spectroscopy (EDS, Tescan Mira 3 MH) and transmission electron microscopy (TEM, JEM 2100F). The surface functional groups were tested by Fourier transform infrared spectrometry (FTIR, Tensor II, Bruker) and X-ray photoelectron spectroscopy (XPS, Thermo Scientific K-Alpha). The crystal structure was investigated by an X-ray diffractometer (XRD, Bruker D8). The ion leaching from prepared biochar during RhB adsorption was measured by inductively coupled plasma optical emission spectrometry (ICP-OES, Agilent 5110).

https://doi.org/10.1021/acsomega.2c06968
ACS Omega 2023, 8, 4813−4825

Finally, the thermostability of samples was detected by a thermogravimetric analyzer (TGA, TA550).

2.4. Batch Adsorption Studies for RhB. *2.4.1. Adsorption Studies.* The influence of ABL biochar dosage on RhB uptake was carried out by adding separately 0.25, 0.5, 0.75, 1, and 1.25 g/L of the adsorbent into flasks with RhB solution. In the initial concentration test, the RhB dye concentration varied from 50 to 250 mg/L. To examine the impact of contact time, the contact time was recorded within 120 min. The effect of pH on RhB adsorption was carried out by adjusting the pH of the solution in the range of 2−12. Each adsorption experiment was conducted in triplicate. The RhB concentration was analyzed using an ultraviolet−visible double beam spectrophotometer at 554 nm (Unico 4802s, China). The adsorption capacity and removal efficiency of the biochar at the equilibrium state can be evaluated using the following equations

$$q_t = \frac{(C_0 - C_e)V}{m} \quad (1)$$

$$R = \frac{C_0 - C_e}{C_0} \quad (2)$$

where q_t (mg/g) is the adsorption capacity at equilibrium, C_0 (mg/L) is the initial concentration of RhB, C_e (mg/L) is the equilibrium concentration after time t, V (L) is the volume, and m (g) is the adsorbent mass used for adsorption.

2.4.2. Adsorption Kinetics. Initially, 0.01 g of obtained ABL biochar was added into 10 mL RhB solution with its concentration of 200 mg/L, taking aliquots at intervals from 30 s to 120 min at 25 °C.

The adsorption kinetics of RhB were separately analyzed by the pseudo-first-order (PFO) model, the pseudo-second-order (PSO) model, and intra-particle diffusion (IPD) models, and the corresponding equations are listed in Table 1.

K_L (L/mg) is the Langmuir constant; Ce (mg/L) is the equilibrium concentration. n is the Freundlich constant about surface heterogeneity; and K_F ($mg^{-1/n}{\cdot}g^{-1}{\cdot}L^{-1/n}$) is the Freundlich constant associated with adsorption capacity. ns is the Sips isotherm model exponent, ad Ks (L/g) is the Sips isotherm model constant.

ΔG (KJ/mol) is the Gibbs energy; K_d is the distribution coefficient for the adsorption; R is the ideal gas constant, whose value is 8.314 J/(mol·K); T (K) is the absolute temperature; ΔH (KJ/mol) is the activated enthalpy; and ΔS is the change in entropy (J/mol/K).

2.4.3. Adsorption Isotherms and Thermal Dynamics. Isotherm experiments were conducted with an initial RhB concentration range of 25−250 mg/L and temperatures at 303, 313, and 323 K, respectively. The adsorption models including the Langmuir model, Freundlich model, Sips model, and thermodynamic model are described separately in Table 1.

2.5. Regeneration Properties. The biochar samples with adsorbed RhB were pyrolyzed up to 500 °C under N_2 flow for 1 h in a tube furnace at a heating rate of 5 °C/min to recover and then to investigate the stability and reusability of the ABL biochar for RhB adsorption.

Table 1. Adsorption Kinetics, Isotherm, and Thermodynamic Models

adsorption model	type	equation[a]	refs
kinetics	PFO	$q_t = q_e(1 - e^{-k_1 t})$	38
	PSO	$q_t = \frac{t}{\frac{1}{k_2 q_e^2} + \frac{t}{q_e}}$	39
	IPD	$q_t = K_i t^{0.5} + C_i$	40
isotherm	Langmuir	$q_e = \frac{q_m K_L C_e}{1 + K_L C_e}$	41
	Freundlich	$q_e = K_F C^{1/n}$	42
	Sips	$q_e = \frac{q_m (K_S C_e)^{ns}}{1 + (K_S C_e)^{ns}}$	43
thermodynamic	van der Hoff equation	$\Delta G = -RT\ lnK_d K_d = \frac{q_e}{C_e} lnK_d = \Delta S/R - \Delta H/RT$	44

[a] q_e (mg/g) and q_t (mg/g) are the adsorption capacities at equilibrium and at time t (min), respectively; k_1 (min^{-1}) is the rate constants of the PFO kinetic model. k_2 ($g{\cdot}mg^{-1}{\cdot}min^{-1}$) is the rate constant of the PSO kinetic model. k_i ($mg{\cdot}min^{0.5}$)/g is the rate constant of the IPD kinetic model; C_i (mg/g) is a constant of boundary layer thickness.

3. RESULTS AND DISCUSSION

3.1. Physical Properties of ABL Residues and Biochar. Table 2 presents the elemental compositions of raw ABL residues and biochar samples. Notably, the C content of residues is 46.13%, indicating that it is favorable for preparing biochar. Compared with the residues, the H and O contents of the biochar samples all decreased, whereas the C content increased sharply, suggesting decomposition and cracking during dehydration and decarboxylation reactions.[45] The decrease in the H/C ratio indicated higher aromaticity,[46] whereas the increased O/C and (O + N)/C ratios implied lower polarity, which might be attributed to the stronger hydrophobicity and fewer surface polar functional groups.[47] Interestingly, the C content of ABL@KOH was the lowest among the biochar samples, indicating a lower carbonization degree.[48] Notably, the O/C and (O + N)/C ratios of the ABL@$ZnCl_2$ and ABL@H_3PO_4 samples were the highest, proving that the samples had the highest polarity and could provide more adsorption sites in the subsequent adsorption experiment, which was conducive to the adsorption process. Moreover, it has been reported that the activation ingredient is one of the determining factors in obtaining high-quality CHM biochar. Figure 2a presents the N_2 adsorption−desorption isotherms of biochar samples at 77 K. Except for the ABL@H_3PO_4 sample, the N_2 adsorption−desorption isotherms of the obtained biochar samples both showed type-I isotherms with small hysteresis, indicating that there were mainly micropores. However, the adsorption−desorption isotherm of the ABL@H_3PO_4 sample displayed a type IV isotherm, implying that only a small number of micropores and a large number of mesopores were present,[49] which were consistent with its pore size distribution (Figures 2b and S1a). As exhibited in Figure 2b, the pore size of ABL@H_3PO_4 was mainly distributed from 1−2 to 4−6 nm, which was much larger than those of other ABL biochars.

Table 3 lists the pore structure parameters of the obtained ABL biochar. Compared with ABL@Blank, the biochar activated using chemical reagents had a large specific surface area and rich pore structures. Evidently, the ABL@$ZnCl_2$ biochar showed the largest BET surface area (1866 m^2/g) and micropore volume (0.47 cm^3/g). Additionally, the total pore volume of the ABL@H_3PO_4 biochar sample was the largest (2.38 cm^3/g), while its micropore volume was the lowest.

After chemical activation, their SEM morphological characteristics changed a lot (Figure S1b). Clearly, the fibrous tissue in

https://doi.org/10.1021/acsomega.2c06968
ACS Omega 2023, 8, 4813−4825

Table 2. Elemental Composition of Raw ABL Residues and Prepared Biochar

samples	C (%)	H (%)	O (%)	N (%)	S (%)	H/C	O/C	(O + N)/C
residues	46.13	4.96	42.26	1.78	0.16	0.11	0.92	0.95
ABL@$ZnCl_2$	73.86	2.82	12.82	3.71	0.21	0.04	0.17	0.22
ABL@H_3PO_4	68.90	2.13	14.76	0.28	0.05	0.03	0.21	0.22
ABL@KOH	63.31	2.04	12.64	0.67	0.30	0.03	0.20	0.21

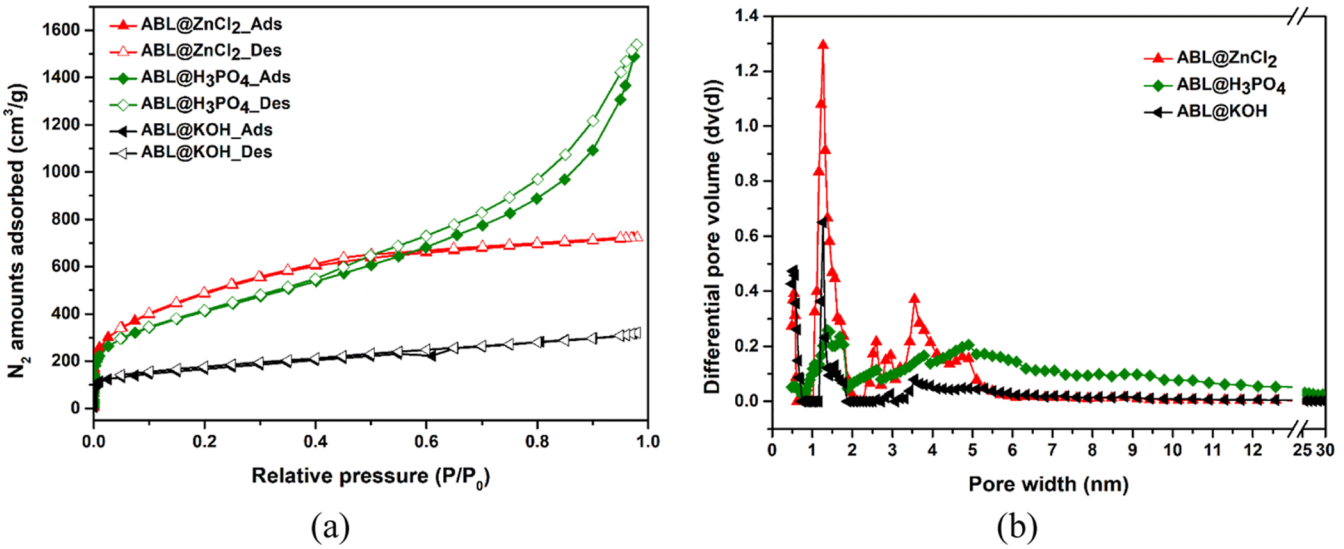

Figure 2. (a) N_2 adsorption−desorption isotherms of biochar samples at 77 K. (b) Nonlocal density functional theory pore size distribution of biochar samples.

Table 3. Pore Structure Parameters of Prepared Biochar

samples	BET (m^2/g)	Langmuir (m^2/g)	micropore volume (cm^3/g)	total pore volume (cm^3/g)	average pore diameter (nm)
ABL@Blank	52	90	not available	0.07	5.44
ABL@$ZnCl_2$	1866	2773	0.47	1.14	2.45
ABL@H_3PO_4	1488	2069	0.03	2.38	6.40
ABL@KOH	590	842	0.10	0.50	3.36

the raw material was destroyed into many small parts. The surface of the ABL@$ZnCl_2$ sample was flat, and the particle size was more uniform. This was because $ZnCl_2$ destroyed cellulose and other macromolecular organics during the pyrolysis process, forming a large number of micropores and mesopores.[50] In contrast, the surface of the ABL@H_3PO_4 sample was relatively rough, and many particles were attached to the surface. Furthermore, there were many macroscopic large holes inside and outside the ABL@KOH biochar, resulting from the gas produced by reacting C with KOH during reaction.[51] Additionally, the EDS mapping (Figure S1c) indicates that the elements were evenly distributed on the surface of obtained ABL biochar samples. A closer look at biochar samples' microstructure can be obtained with TEM images (Figure S1d,e). As compared to ABL@H_3PO_4, ABL@$ZnCl_2$ had smaller and more uniform pores, while ABL@KOH had fewer micropores, which was consistent with the analysis of the pore structure.

Thermogravimetric analysis of the ABL biochar revealed that they all have good thermal stability (Figure S2a,b). When heated to 800 °C, their weight loss was only about 10−15%, attributing to the degradation of cellulose and hemicellulose.[52] In the initial stage of the drying process, the weight loss may be due to the volatilization of some residual chemicals during the preparation process.[53]

3.2. Adsorption Performance Evaluation. *3.2.1. Effect of Adsorbent Dosage.* Figure 3a presents the effect of biochar dosage on RhB removal efficiency. Notably, with an increase in biochar dosage, the removal rate of RhB also gradually increased, except for the ABL@KOH biochar. When the dosage of ABL biochar was 1.25 g/L, the RhB removal rates were both higher than 85%. Intriguingly, when the adsorbent mass was 1.0 g/L, the removal rate of RhB was comparable to that of 1.25 g/L adsorbent. The results suggested that the optimum adsorbent dosage was 1.0 g/L, ensuring a relatively good removal rate and low cost.

3.2.2. Effect of Contact Time. Figure 3b,c shows the effect of the contact time of the ABL biochar on the removal efficiency as well as the adsorption capacity of RhB. Evidently, at the onset of adsorption (10 min), the amount of RhB adsorbed on the adsorbents increased rapidly, then increased slowly, and finally reached equilibrium. Furthermore, the removal efficiency and adsorption capacity of the ABL@H_3PO_4 sample at the initial stage were clearly much higher than those of the ABL@$ZnCl_2$ sample because of the larger pore size of the H_3PO_4-activated biochar. After 20 min, the adsorption capacity gradually leveled off until equilibrium was reached. Finally, the RhB removal rate and adsorption capacity of two samples were separately greater than 90% and 180 mg/g, and the sample with a higher removal rate and adsorption capacity was obtained from ABL@$ZnCl_2$, reaching 95% and 190.63 mg/g, respectively.

3.2.3. Effect of Dye Concentration. Figure 3d,e demonstrates the effect of the initial RhB concentration on the adsorption performance. When the initial RhB concentration was increased, the RhB removal efficiency decreased while the adsorption capacity gradually increased. As it can be noted, when the initial

https://doi.org/10.1021/acsomega.2c06968
ACS Omega 2023, 8, 4813−4825

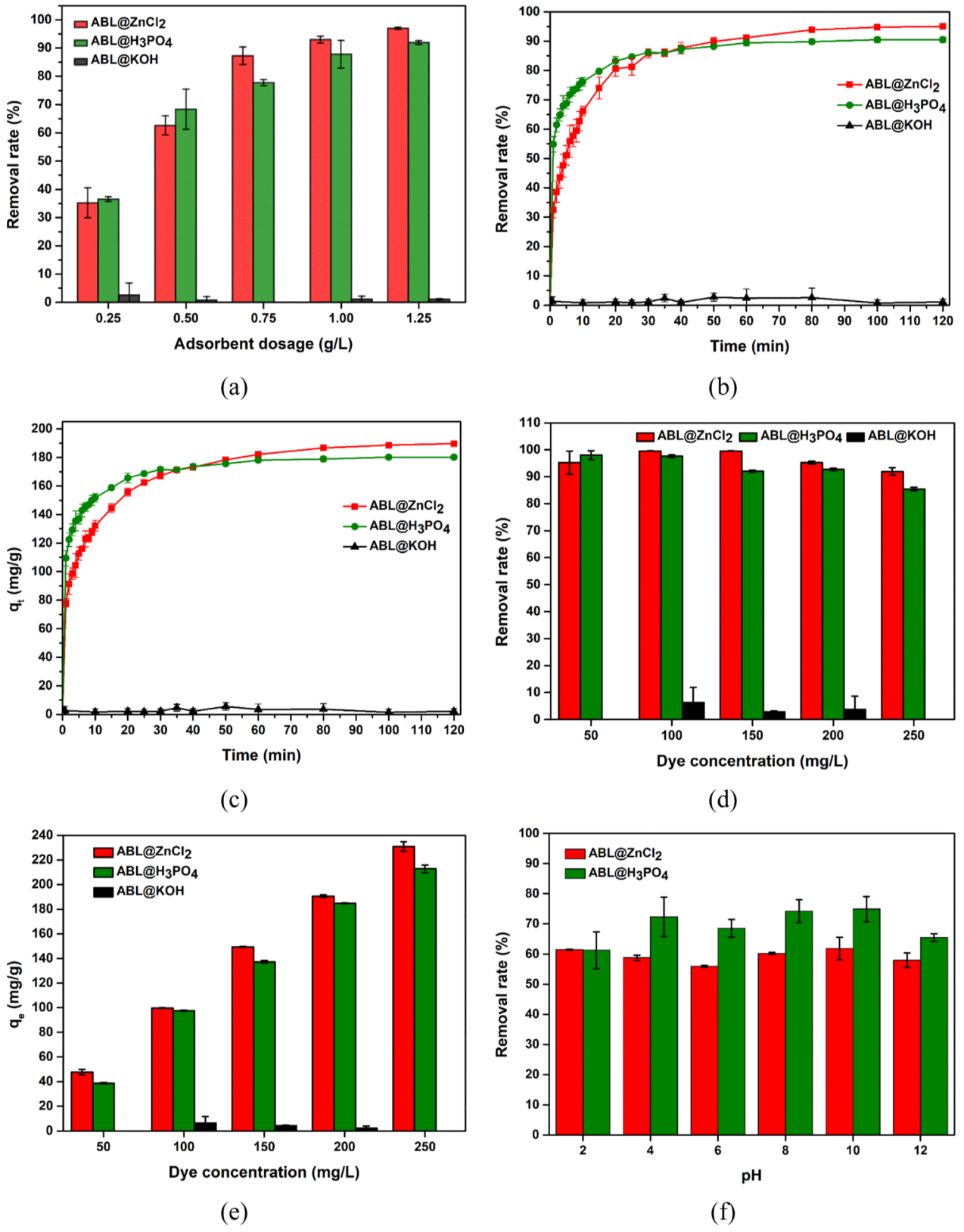

Figure 3. (a) Effect of adsorbent dosage on the removal efficiency of RhB (initial concentration 200 mg/L, contact time 20 min); Effect of contact time on the (b) removal efficiency of the sample and (c) on the adsorption capacity adsorbed RhB (initial concentration 200 mg/L, adsorbent dosage 1 g/L); effect of the RhB concentration on the (d) removal efficiency and (e) adsorption capacity (adsorbent dosage 1 g/L, contact time 120 min); (f) effect of pH on the removal efficiency of RhB (initial concentration 200 mg/L, adsorbent dosage 1 g/L, contact time 20 min).

RhB concentration was 250 mg/L, the RhB removal efficiency of all samples decreased remarkably, which is in agreement with previous studies.[54] However, the ABL@KOH sample showed no change in adsorption, even at a high initial dye concentration.

https://doi.org/10.1021/acsomega.2c06968
ACS Omega 2023, 8, 4813−4825

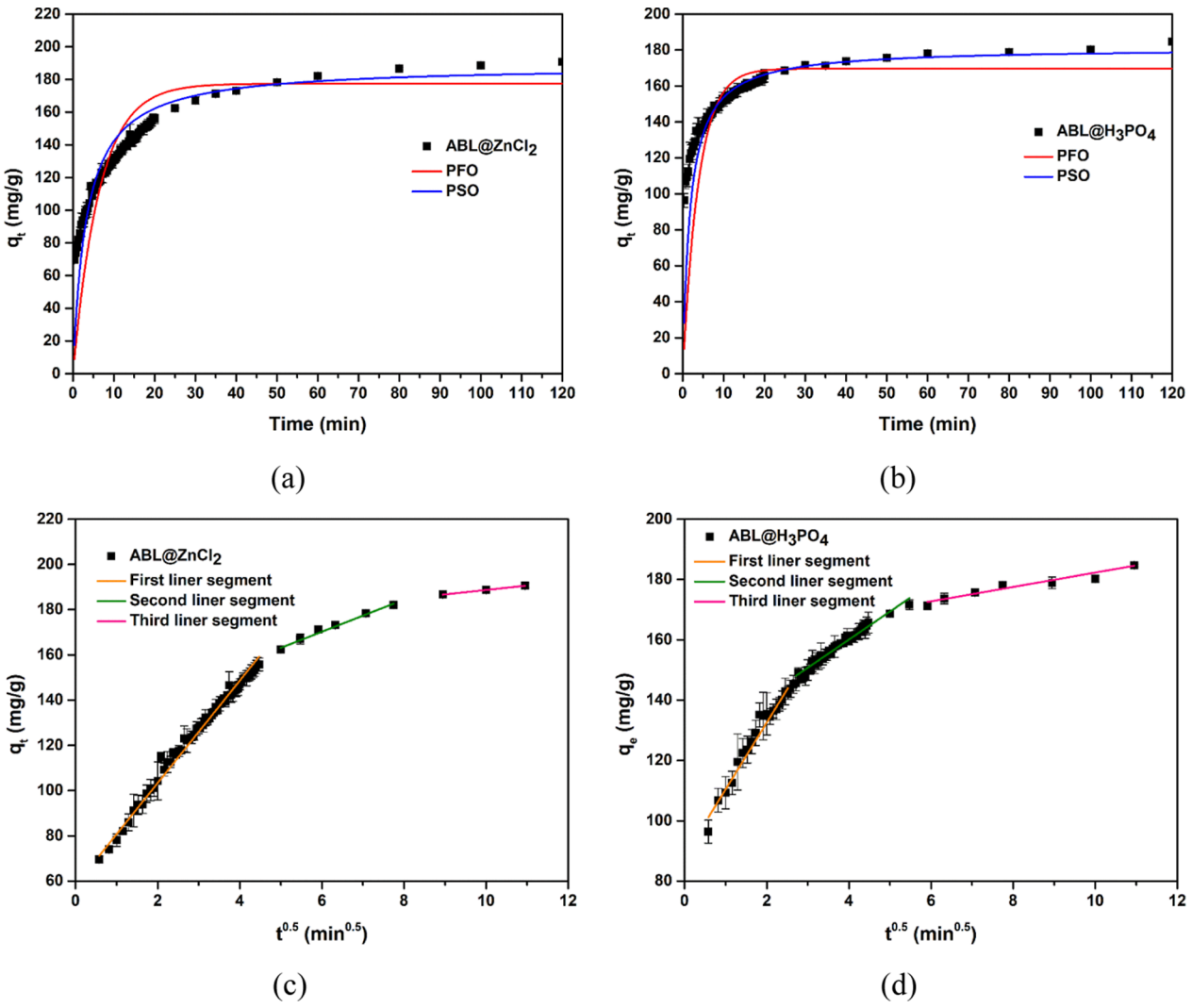

Figure 4. PFO and PSO adsorption kinetic models of RhB adsorption by (a) ABL@$ZnCl_2$ and (b) ABL@H_3PO_4; IPD adsorption kinetic study of RhB adsorption by (c) ABL@$ZnCl_2$ and (d) ABL@H_3PO_4.

Table 4. Kinetic Constants of PFO and PSO Models

		PFO				PSO			
Sample	$q_{e,exp}$(mg/g)	K_1 (min^{-1})	q_e(mg/g)	R^2	SSE[a]	K_2(g/mg/min)	q_e(mg/g)	R^2	SSE
ABL@$ZnCl_2$	190.63	0.00258	177.40	0.73	1.59	0.000027	188.69	0.88	0.23
ABL@H_3PO_4	184.70	0.00426	169.66	0.27	1.81	0.000051	181.24	0.81	0.42

[a]SSE: sum of the squared error.

Hence, it was not considered in the next exploration of kinetics and isotherms.

3.2.4. Effect of pH. Figure 3f shows the effect of the pH value on RhB removal efficiency. Evidently, there was a less significant effect of pH change on the removal rate of RhB. Considering the cost, the pH of the solution (≈6) will not be changed in the subsequent adsorption experiments.

3.2.5. Adsorption Kinetics. To determine the adsorption rate of RhB on the ABL biochar, it was necessary to determine their mass transfer coefficients. Figure 4a,b and Table 4 show that the fitting data R^2 of the PSO kinetic model for all samples were higher than those of the PFO kinetic model, which proves that the PSO kinetic model better describes the RhB adsorption process.

Moreover, the IPD model was employed to explain the adsorption process of RhB on ABL biochar. It should be noted that the entire RhB adsorption process can be divided into three stages (Figure 4c,d). During the first stage (bulk diffusion), RhB adsorption was achieved through rapid boundary layer diffusion to the external surface. Especially, the C_i value of ABL@H_3PO_4 (88.31 mg/g) was far higher than that of ABL@$ZnCl_2$ (58.08 mg/g), indicating that ABL@H_3PO_4 has a greater boundary layer diffusion effect. Subsequently, the RhB molecules gradually diffused into the porous structure of the ABL biochar in the second stage (film diffusion). Finally, the adsorption process gradually reached equilibrium in the third stage (pore diffusion). Although IPD was involved in the adsorption process, due to the fitting line not passing through the origin, IPD was not the only

https://doi.org/10.1021/acsomega.2c06968
ACS Omega 2023, 8, 4813−4825

Table 5. Kinetic Constants for the Intraparticle Diffusion Model

	first liner segment			second liner segment			third liner segment		
sample	K_{id}(mg/g/h$^{0.5}$)	C_i(mg/g)	R^2	K_{id}(mg/g/h$^{0.5}$)	C_i(mg/g)	R^2	K_{id}(mg/g/h$^{0.5}$)	C_i(mg/g)	R^2
ABL@ZnCl2	22.62	58.08	0.99	7.11	127.54	0.99	1.96	169.06	0.99
ABL@H3PO4	22.12	88.31	0.97	9.30	122.83	0.97	2.39	158.41	0.97

Table 6. Constants for the Isotherm Model

	Langmuir model			Freundlich model			Sips model			
sample	q_e(mg/g)	K_L(L/mg)	R^2	K_F [(mg^{1-n} L^n)/g]	n	R^2	q_e(mg/g)	K_S(L/mg)	ns	R^2
ABL@ZnCl2	263.19	0.12	0.89	44.05	2.19	0.83	192.41	0.23	2.31	0.92
ABL@H3PO4	309.11	0.04	0.72	20.60	1.67	0.68	186.82	0.09	2.25	0.74

Table 7. Comparison of the Maximum Adsorption Capacity of RhB Dye on Biochar Obtained from Other Biomass

raw material	BET (m^2/g)	total pore volume (cm^3/g)	adsorbent dosage (g/L)	dye concentration (mg/L)	q_e(mg/g)	refs
stalk corn			2.5	10−50	5.300	11
MOF-5/COF	7.025		0.8	5−25	16.18	57
tapioca peel waste	146		2	25−150	33.10	36
porous organic polymers	4.28	0.038	0.3	5−30	59.20	58
rabbit manure	42.66	0.138	0.9	20−80	65.03	59
bamboo shoot shell	513	0.27	1	2−300	85.80	60
cassava slag	3			25−500	105.3	44
white sugar	1145	0.53	0.8	25−100	123.5	54
olive			0.7	50−250	263.7	61
	1866 (ABL@$ZnCl_2$)	1.143			263.19	
ABL residue	1488 (ABL@H_3PO_4)	2.382	1	50−250	309.11	this study

Table 8. Thermodynamic Parameters for RhB Adsorption

sample	ΔG(kJ/mol)				ΔH(kJ/mol)	ΔS(J/mol/K)
	298 K	308 K	318 K	328 K		
ABL@ZnCl2	−8.06	−8.34	−9.28	−9.80	19.80	92.60
ABL@H3PO4	−3.31	−4.76	−5.60	−6.09	35.78	111.47

speed-limiting step.[10,55] All these processes can be verified by the obtained K value in Table 5.

3.2.6. Adsorption Isotherm. To delineate the adsorption of RhB on the ABL biochar samples, Langmuir, Freundlich, and Sips models were used to fit the isotherms (Figure S3). Table 6 lists the fitting parameters for RhB adsorption with different models. Notably, the correlation coefficient of RhB adsorption isotherms using the Sips model was the highest, suggesting that the Sips model was suitable to describe the adsorption behavior of the obtained biochar.[56] Evidently, the ns value of the ABL@H_3PO_4 was the lowest at 2.25, indicating that the sample had systematic heterogeneity. In addition, the maximum RhB adsorption capacity of ABL biochar can reach 309.11 mg/g, which belonged to one of the best RhB adsorbents, as presented in Table 7.

3.2.7. Thermodynamic Analysis. Furthermore, the thermodynamic analysis was conducted to determine enthalpy (ΔH), entropy (ΔS), and Gibbs free energy (ΔG) using the equation listed in Table 1. As illustrated in Figure S3c,d, charts of ln K_d versus 1/T were plotted, from which thermodynamic parameters were calculated and listed in Table 8. Evidently, all ΔG values were negative, indicating that the RhB adsorption on ABL@$ZnCl_2$ and ABL@H_3PO_4 both took place spontaneously. Besides, the absolute ΔG value increased with the increase of temperature, suggesting that higher temperature was beneficial to the adsorption process. The positive values of ΔH implied that the RhB adsorption processes on ABL@$ZnCl_2$ (19.80 KJ/mol) and ABL@H_3PO_4 (35.78 KJ/mol) were both endothermic, and the positive ΔS values demonstrated increased randomness and disorderliness at the solid/liquid interface during RhB adsorption.

3.3. Adsorption Mechanism. *3.3.1. FTIR.* It can be noted that the FTIR characteristic absorption peaks of the ABL biochar were basically consistent with ABL@Blank (Figure 5a). However, some differences were observed. First, for all biochar samples, the newly appearing peak at 1571 cm^{-1} was ascribed to the stretching vibration of C═O and C═C of the aromatic ring. This favorable structure may produce an EDA effect ($\pi-\pi$ electron donor−acceptor interaction) between the biochar and adsorbed substances in adsorption experiments.[62] Second, for the ABL@$ZnCl_2$ sample, the peak at 1145 cm^{-1} was assigned to the O−H bond of phenolic compounds.[63] The peak at 1384 cm^{-1} of the ABL@H_3PO_4 sample was attributed to −COOH and O−H bonds. The peak at 1169 cm^{-1} was attributed to the stretching vibrations of P═O and O−C, indicating that there may be a P−O−C, P═OOH structure in the sample.[64] These oxygen-containing functional groups could form hydrogen bonds with RhB molecules, which are beneficial for the subsequent adsorption process. The peak at 1433 cm^{-1} of the ABL@KOH sample may be attributed to the aromatic ring structure. The peaks at 1074 and 1046 cm^{-1} were assigned to C−H bending of the alkene and C−O−C stretching.[65]

3.3.2. XPS. Figures 5b−d and S4 show the XPS spectra of all ABL biochar. Several interesting phenomena can be observed.

https://doi.org/10.1021/acsomega.2c06968
ACS Omega 2023, 8, 4813−4825

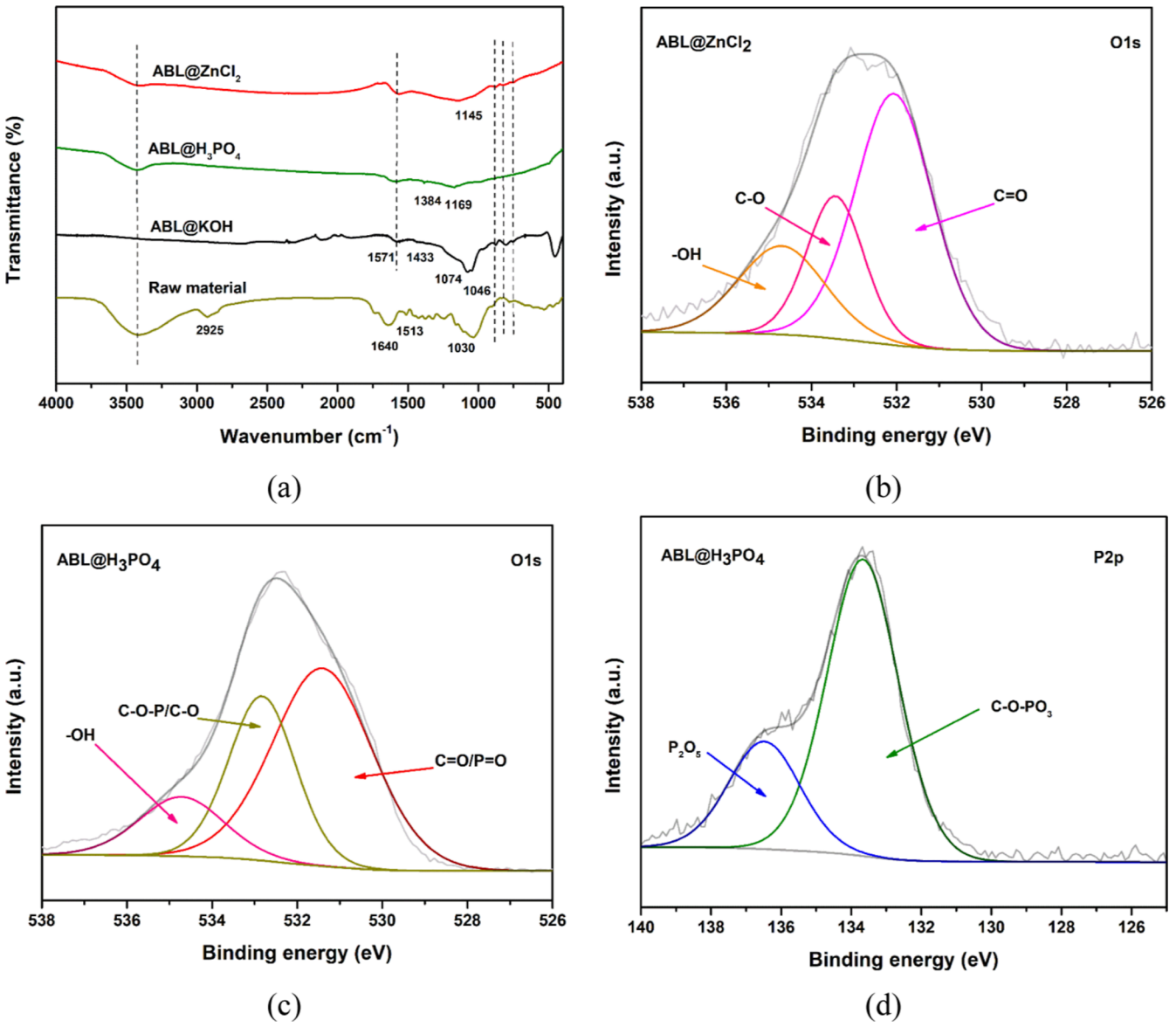

Figure 5. (a) FTIR spectra of all biochar and raw material; (b) O 1s XPS analysis of ABL@$ZnCl_2$, (c) O 1s XPS analysis of ABL@H_3PO_4; and (d) P2p XPS analysis of ABL@H_3PO_4.

First, the O 1s XPS spectra of the ABL@$ZnCl_2$ sample were divided into three peaks at 529.93, 532.09, and 534.52 eV, which can be attributed to C═O, C−O, and −OH, respectively. However, the oxygen-containing functional groups of the ABL@H_3PO_4 sample mainly included C═O/P═O, C−O−P/C−O, and −OH, which are both favorable for the adsorption of dyes. In contrast, the oxygen-containing functional groups of ABL@KOH sample were only −OH and R−COO, which may not play a significant role in the adsorption process.[66] Second, the C 1s XPS spectra of all samples had three peaks at 284.48, 285.70, and 288.95 eV, corresponding to C−C/C−H, C−O, and O═C−O, respectively. Third, the N 1s XPS spectra of the ABL@$ZnCl_2$ and ABL@H_3PO_4 samples were divided into two main peaks, corresponding to pyridine-N and pyrrole-N, respectively. Fourth, the peaks of the Zn 2p XPS spectra of the ABL@$ZnCl_2$ sample corresponded to Zn 2p1/2 and Zn 2p3/2 of ZnO, which were consistent with the XRD results, indicating that ZnO was formed during the activation of $ZnCl_2$. Finally, for the ABL@H_3PO_4 sample, there were two peaks at 136.48 and 133.68 eV, which split into the P 2p. These peaks represent C−O−PO_3 and P_2O_5, which can promote the adsorption process.[54] Compared with ABL@Blank, the ABL biochar samples had more oxygen-containing functional groups and provided more active sites for subsequent adsorption.

3.3.3. XRD Analysis and Stability of ABL@$ZnCl_2$ and ABL@H_3PO_4. The XRD patterns of obtained ABL biochar all have 002 ($2\theta = 24°$) and 100 ($2\theta = 44°$) wide reflections, indicating that they are amorphous biochar caused by the accumulation of an aromatic layer structure,[67] as shown in Figure 6a. The peaks of the ABL@$ZnCl_2$ sample at 2θ = 31.8, 34.4, and 36.3° correspond to those of ZnO, confirming the formation of $Zn_5(OH)_8Cl_2$ and subsequent ZnO.[68] However, the peaks of ABL@H_3PO_4 biochar at 23.1, 24.2, 26.7, 31.6, and 37.6° all corresponded to phosphoric acid and its hydrate. The peaks at 15.1 and 27.4° were attributed to phosphate radicals, which resulted from the catalytic dehydration reaction.[69] Notably, the amorphous structures of ABL@$ZnCl_2$ and ABL@H_3PO_4 showed almost no change after RhB adsorption, suggesting

https://doi.org/10.1021/acsomega.2c06968
ACS Omega 2023, 8, 4813−4825

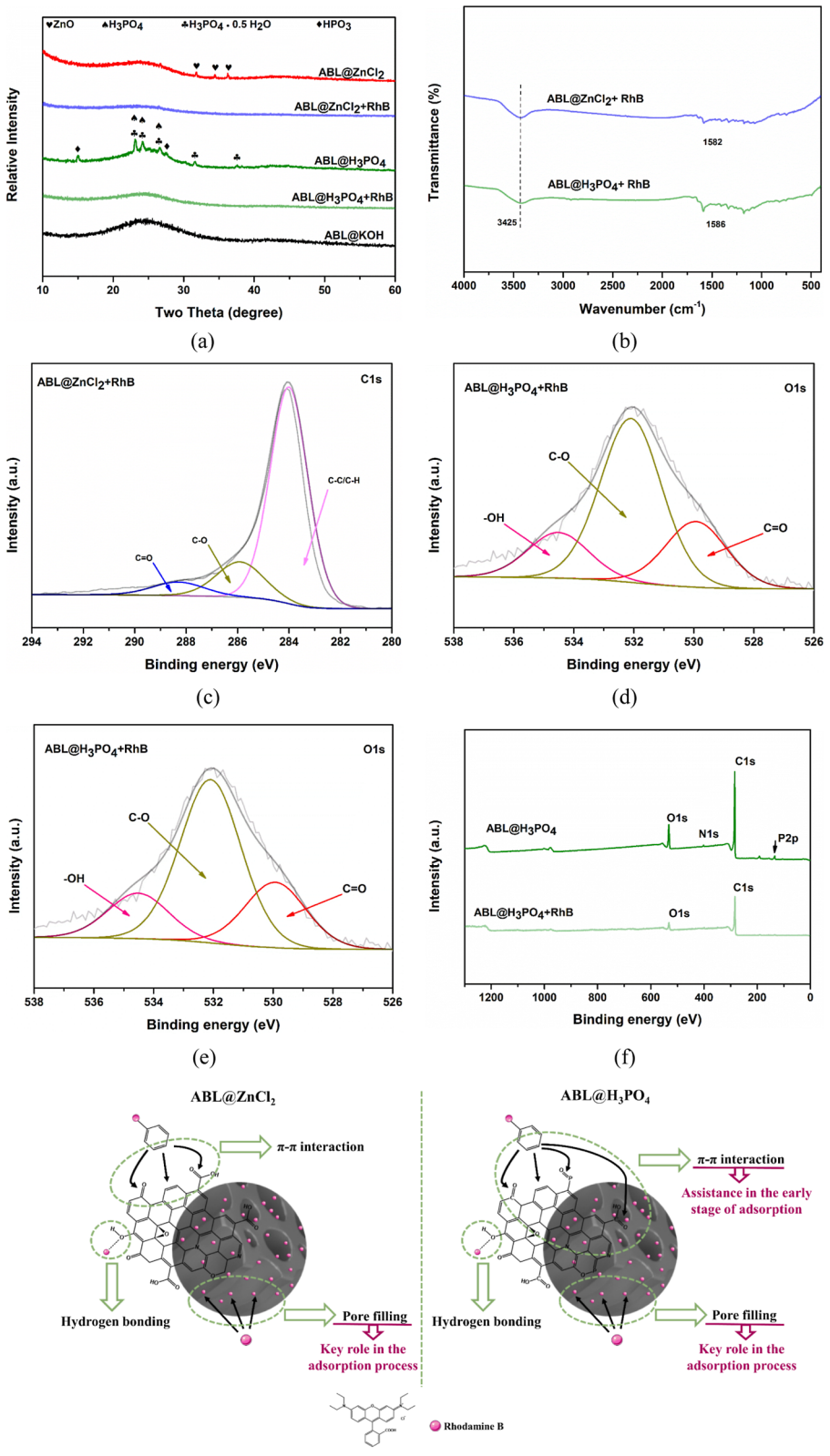

Figure 6. (a) XRD patterns of biochar samples before and after RhB adsorption. (b) FTIR spectra of biochar samples after adsorption. (c) C 1s, (d) O 1s XPS analysis of ABL@$ZnCl_2$ after RhB adsorption, (e) O 1s, (f) XPS spectra of ABL@H_3PO_4 and ABL@H_3PO_4 after RhB adsorption. (g) RhB adsorption mechanism of ABL@$ZnCl_2$ and ABL@H_3PO_4.

the biochars after RhB adsorption were fairly stable. Table S5 lists the concentrations of the ions leached from prepared biochar during the RhB adsorption process. Although ZnO (attached to the ABL@$ZnCl_2$ surface) and phosphoric acid (attached to the ABL@H_3PO_4 surface) were detected in the solution after RhB adsorption, all leached ions were very small,

https://doi.org/10.1021/acsomega.2c06968
ACS Omega 2023, 8, 4813−4825

Table 9. Cost and Economic Value of Biochar Used in Industrial Wastewater Production ($/t)

sample	raw material	disposal cost	chemical reagents	energy consumption	wages of workers	total cost	commercial biochar price	pay back
ABL@$ZnCl_2$	1.5	15.3	45.8	612.4	366	1041	2013	972
ABL@H_3PO_4			30.5			1026		987

demonstrating the feasibility of adsorbing RhB with ABL@$ZnCl_2$ and ABL@H_3PO_4.

3.3.4. Proposed Adsorption Mechanism of RhB on ABL@$ZnCl_2$ and ABL@H_3PO_4. To further examine the adsorption mechanism of RhB on the ABL biochar, FTIR and XPS spectra of the biochar after adsorption were obtained (Figures 6b−f and S5). The position of the carbonyl peak changed from 1571 to 1582 and 1586 cm^{-1} after RhB adsorption on ABL@$ZnCl_2$ and ABL@H_3PO_4 biochar, respectively, proving that the $\pi-\pi$ electron donor−acceptor interaction occurred with the participation of functional groups in the adsorption process.[58] The XPS analysis of the biochar after RhB adsorption showed that the C 1s, N 1s, and O 1s peaks of the ABL@$ZnCl_2$ biochar all changed, indicating that C−O bonds, C═O bonds, and N-containing functional groups participated in the adsorption process. In addition, the P 2p peak was weaker after the RhB uptake, suggesting that the P−O−P bond and P-containing functional groups of the ABL@H_3PO_4 biochar also play important roles in adsorption.[44] In contrast to the larger BET surface area and micropore volume of ABL@$ZnCl_2$, at the early stage of adsorption, the RhB removal rate and adsorption capacity on ABL@H_3PO_4 were even higher, which was owing to its larger pore diameter (6.40 nm) and the EDA effect caused by the abundant P-containing functional groups of ABL@H_3PO_4. Nevertheless, at the end of the RhB adsorption process, the removal rate and adsorption capacity of ABL@$ZnCl_2$ were finally higher than those of ABL@H_3PO_4, indicating that pore diffusion played a key role in the adsorption process. From the above discussion, Figure 6g shows the schematic diagram of the RhB adsorption mechanism on ABL@$ZnCl_2$ and ABL@H_3PO_4. It can be inferred that pore diffusion, $\pi-\pi$ interactions, and hydrogen bonding all play roles in the physical adsorption of RhB on ABL biochar. $\pi-\pi$ interactions dominated in the early stage of RhB adsorption on ABL@H_3PO_4, while pore diffusion played a crucial role in the whole adsorption process on both adsorbents.

3.3.5. Discussion on ABL@KOH. One thing that should be mentioned is that the adsorption property of RhB on ABL@KOH is very poor. The speculated reasons are as follows: (1) during the preparation of ABL@KOH biochar, there will be a large amount of gas generated due to the reaction of KOH with carbon at high temperature, resulting in many large holes inside and outside the ABL@KOH biochar with extremely light weight. Therefore, the interaction between RhB dye and the pore surface was not strong enough. (2) The stable aromatic ring structure of ABL@KOH cannot provide too many active sites for RhB adsorption.

3.4. Industrial Economic Feasibility Analysis. Economic analysis is an important factor in practical applications. Figure S6 shows the poor RhB adsorption capacity of commercial biochar used for wastewater treatment compared to that of ABL$ZnCl_2$ and ABL@H_3PO_4. Furthermore, Table S6 also provides a comparison of biochar cost with other materials. It is evident that ABL@$ZnCl_2$ and ABL@H_3PO_4 biochars are very competitive in terms of cost.[70,71] Table 9 lists the production costs and prices required based on the energy consumption for our work. It can be clearly seen that the pay back of our ABL biochar was USD 972/t (ABL@$ZnCl_2$) and USD 987/t (ABL@H_3PO_4) compared to commercial biochar, suggesting that it is feasible to prepare biochar from ABL residues in industry.

3.5. Regeneration Evaluation. The regeneration capacities of the different samples after five cycles are shown in Figure 7. Compared with the first cycle, the ABL@$ZnCl_2$ sample

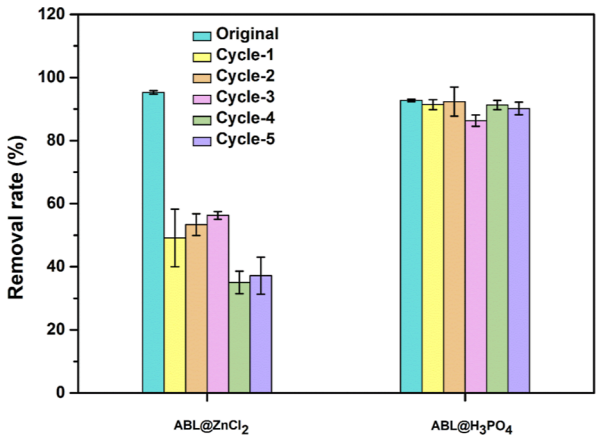

Figure 7. Five adsorption−desorption cycles of RhB on the obtained biochar samples.

exhibited a certain downward trend, but there was still a 37% removal rate after five cycles. Speculatively, as a result of the smaller average pore diameter (2.45 nm) of ABL@$ZnCl_2$, the original microporous structure collapsed, resulting in inactivation after further carbonization regeneration. In contrast, the ABL@H_3PO_4 sample displayed excellent RhB removal ability after five cycles, which was only slightly different from the first cycle, indicating that this biochar has remarkable reusability and stability.

4. CONCLUSIONS

In summary, we had successfully prepared ABL@$ZnCl_2$ (1866 m^2/g), ABL@H_3PO_4 (1488 m^2/g), and ABL@KOH (590 m^2/g) with an ultrahigh specific surface area. Through pore diffusion, $\pi-\pi$ interaction, and hydrogen bonding, ABL biochar had excellent adsorption performance for RhB. Moreover, when C_0 was 200 mg/L, biochar dosage was 1g/L, and the contact time was 120 min, the maximum RhB adsorption capacity and removal efficiency on ABL@$ZnCl_2$ and ABL@H_3PO_4 were 190.63 mg/g, 95% and 184.70 mg/g, 92%, respectively, indicating that it was feasible to prepare biochar from the ABL residue for RhB adsorption. Further analysis showed that the adsorption data were in accordance with PSO kinetics and Langmuir isotherm models, and the theoretical maximum adsorption capacities of ABL@$ZnCl_2$ and ABL@H_3PO_4 for RhB were 263.19 and 309.11 mg/g, respectively. Additionally, pore diffusion, $\pi-\pi$ interactions, and hydrogen bonding all play roles in the physical adsorption of RhB on ABL biochar. $\pi-\pi$ interactions dominated in the early stage of RhB adsorption on ABL@H_3PO_4, while pore diffusion played a crucial role in the whole adsorption process on both adsorbents. In addition, the prepared biochar showed good economic applicability, with

https://doi.org/10.1021/acsomega.2c06968
ACS Omega 2023, 8, 4813−4825

recovery rates of USD 972/t (ABL@$ZnCl_2$) and USD 987/t (ABL@H_3PO_4), respectively. More importantly, even after five cycles, ABL@H_3PO_4 biochar still showed great RhB removal efficiency, suggesting that it had a good application prospect and provided a new method for the resource utilization of traditional CHM residues. However, there might be some potential environmental pollution associated with the preparation of ABL@$ZnCl_2$ and ABL@H_3PO_4 biochars. In our future work, a variety of green technologies will be investigated for the preparation of CHM biochar.

■ ASSOCIATED CONTENT

Supporting Information

The Supporting Information is available free of charge at https://pubs.acs.org/doi/10.1021/acsomega.2c06968.

Characterization results including pore structure analysis, SEM, SEM-EDS mapping, TEM, TGA, XPS, FTIR, and XRD; nonlinear fitting of Langmuir, Freundlich, and Sips models for RhB adsorption; and table showing the concentrations of the ions leached after RhB adsorption (PDF)

■ AUTHOR INFORMATION

Corresponding Author

Zhijuan Zhang − *College of Pharmacy, Henan University of Chinese Medicine, Zhengzhou 450046, China; Institute of Mass Spectrometer and Atmospheric Environment, Jinan University, Guangzhou 510632, China;* orcid.org/0000-0002-9451-2394; Email: zhangyan0204@126.com

Authors

Pengwei Li − *College of Pharmacy, Henan University of Chinese Medicine, Zhengzhou 450046, China*

Ting Zhao − *College of Pharmacy, Henan University of Chinese Medicine, Zhengzhou 450046, China*

Ziheng Zhao − *College of Pharmacy, Henan University of Chinese Medicine, Zhengzhou 450046, China*

Hanxiao Tang − *College of Chinese Medical Sciences, Henan University of Chinese Medicine, Zhengzhou 450046, China*

Weisheng Feng − *College of Pharmacy, Henan University of Chinese Medicine, Zhengzhou 450046, China*

Complete contact information is available at: https://pubs.acs.org/10.1021/acsomega.2c06968

Author Contributions

P.L. and T.Z. contributed equally to this paper. P.L.: supervision, validation, and methodology. T.Z.: investigation and writing-original draft. Z.Z.: formal analysis. H.T.: validation. W.F.: supervision. Z.Z.: supervision, writing-review & editing, and funding acquisition.

Notes

The authors declare no competing financial interest.

■ ACKNOWLEDGMENTS

The authors thank the National Natural Science Foundation of China (grant 21878122) and Pearl River Nova Program of Guangzhou (grant 201710010053) for financial support.

■ REFERENCES

(1) Sillanpää, M.; Mahvi, A. H.; Balarak, D.; Khatibi, A. D. Adsorption of Acid orange 7 dyes from aqueous solution using Polypyrrole/nanosilica composite: Experimental and modelling. *Int. J. Environ. Anal. Chem.* **2023**, *103*, 212−229.

(2) Hayati, B.; Mahmoodi, N. M.; Arami, M.; Mazaheri, F. Dye Removal from Colored Textile Wastewater by Poly(propylene imine) Dendrimer: Operational Parameters and Isotherm Studies. *Clean: Soil, Air, Water* **2011**, *39*, 673−679.

(3) Arami, M.; Rahimi, S.; Mivehie, L.; Mazaheri, F.; Mahmoodi, N. M. Degumming of Persian silk with mixed proteolytic enzymes. *J. Appl. Polym. Sci.* **2007**, *106*, 267−275.

(4) Zhang, X.; Tian, J.; Wang, P.; Liu, T.; Ahmad, M.; Zhang, T.; Guo, J.; Xiao, H.; Song, J. Highly-efficient nitrogen self-doped biochar for versatile dyes' removal prepared from soybean cake via a simple dual-templating approach and associated thermodynamics. *J. Cleaner Prod.* **2022**, *332*, 130069.

(5) Al-Musawi, T. J.; Mengelizadeh, N.; Al Rawi, O.; Balarak, D. Capacity and Modeling of Acid Blue 113 Dye Adsorption onto Chitosan Magnetized by Fe_2O_3 Nanoparticles. *J. Polym. Environ.* **2021**, *30*, 344−359.

(6) Almasian, A.; Mahmoodi, N. M.; Olya, M. E. Tectomer grafted nanofiber: Synthesis, characterization and dye removal ability from multicomponent system. *J. Ind. Eng. Chem.* **2015**, *32*, 85−98.

(7) Mahmoodi, N. M.; Bashiri, M.; Moeen, S. J. Synthesis of nickel-zinc ferrite magnetic nanoparticle and dye degradation using photocatalytic ozonation. *Mater. Res. Bull.* **2012**, *47*, 4403−4408.

(8) Al-Musawi, T. J.; McKay, G.; Rajiv, P.; Mengelizadeh, N.; Balarak, D. Efficient sonophotocatalytic degradation of acid blue 113 dye using a hybrid nanocomposite of $CoFe_2O_4$ nanoparticles loaded on multi-walled carbon nanotubes. *J. Photochem. Photobiol., A* **2022**, *424*, 113617.

(9) Asefi, D.; Mahmoodi, N. M.; Arami, M. Effect of nonionic co-surfactants on corrosion inhibition effect of cationic gemini surfactant. *Colloids Surf., A* **2010**, *355*, 183−186.

(10) Balarak, D.; Zafariyan, M.; Igwegbe, C. A.; Onyechi, K. K.; Ighalo, J. O. Adsorption of Acid Blue 92 Dye from Aqueous Solutions by Single-Walled Carbon Nanotubes: Isothermal, Kinetic, and Thermodynamic Studies. *Environ. Processes* **2021**, *8*, 869−888.

(11) Mousavi, S. A.; Kamarehie, B.; Almasi, A.; Darvishmotevalli, M.; Salari, M.; Moradnia, M.; Azimi, F.; Ghaderpoori, M.; Neyazi, Z.; Karami, M. A. Removal of Rhodamine B from aqueous solution by stalk corn activated carbon: adsorption and kinetic study. *Biomass Convers. Biorefin.* **2021**, DOI: 10.1007/s13399-021-01628-1.

(12) Mahmoodi, N. M.; Ghezelbash, M.; Shabanian, M.; Aryanasab, F.; Saeb, M. R. Efficient removal of cationic dyes from colored wastewaters by dithiocarbamate-functionalized graphene oxide nanosheets: From synthesis to detailed kinetics studies. *J. Taiwan Inst. Chem. Eng.* **2017**, *81*, 239−246.

(13) da Rosa, A. L. D.; Carissimi, E.; Dotto, G. L.; Sander, H.; Feris, L. A. Biosorption of rhodamine B dye from dyeing stones effluents using the green microalgae Chlorella pyrenoidosa. *J. Cleaner Prod.* **2018**, *198*, 1302−1310.

(14) Yilmaz, M.; Mengelizadeh, N.; Saloot, M. k.; shahbaksh, S.; Balarak, D. Facile synthesis of Fe_3O_4/ZnO/GO photocatalysts for decolorization of acid blue 113 under solar, visible and UV lights. *Mater. Sci. Semicond. Process.* **2022**, *144*, 106593.

(15) Mahmoodi, N. M.; Arami, M.; Limaee, N. Y.; Gharanjig, K.; Ardejani, F. D. Decolorization and mineralization of textile dyes at solution bulk by heterogeneous nanophotocatalysis using immobilized nanoparticles of titanium dioxide. *Colloids Surf., A* **2006**, *290*, 125−131.

(16) Mousavi, S. R.; Asghari, M.; Mahmoodi, N. M. Chitosan-wrapped multiwalled carbon nanotube as filler within PEBA thin film nanocomposite (TFN) membrane to improve dye removal. *Carbohydr. Polym.* **2020**, *237*, 116128.

(17) Okoniewska, E. Removal of Selected Dyes on Activated Carbons. *Sustainability* **2021**, *13*, 4300.

(18) Hosseini, F.; Sadighian, S.; Hosseini-Monfared, H.; Mahmoodi, N. M. Dye removal and kinetics of adsorption by magnetic chitosan nanoparticles. *Desalin. Water Treat.* **2016**, *57*, 24378−24386.

(19) Mahmoodi, N. M.; Oveisi, M.; Bakhtiari, M.; Hayati, B.; Shekarchi, A. A.; Bagheri, A.; Rahimi, S. Environmentally friendly ultrasound-assisted synthesis of magnetic zeolitic imidazolate frame-

work - Graphene oxide nanocomposites and pollutant removal from water. *J. Mol. Liq.* **2019**, *282*, 115−130.
(20) Cao, J.; Wang, P.; Shen, J.; Sun, Q. Core-shell Fe_3O_4@zeolite NaA as an Adsorbent for Cu^{2+}. *Materials* **2020**, *13*, 5047.
(21) Sarkar, A.; Adhikary, A.; Mandal, A.; Chakraborty, T.; Das, D. Zn-BTC MOF as an Adsorbent for Iodine Uptake and Organic Dye Degradation. *Cryst. Growth Des.* **2020**, *20*, 7833−7839.
(22) Gao, Y.; Zhang, J.; Chen, C.; Du, Y.; Teng, G.; Wu, Z. Functional biochar fabricated from waste red mud and corn straw in China for acidic dye wastewater treatment. *J. Cleaner Prod.* **2021**, *320*, 128887.
(23) Hayati, B.; Mahmoodi, N. M.; Maleki, A. Dendrimer-titania nanocomposite: synthesis and dye-removal capacity. *Res. Chem. Intermed.* **2013**, *41*, 3743−3757.
(24) Almasian, A.; Olya, M. E.; Mahmoodi, N. M. Preparation and adsorption behavior of diethylenetriamine/polyacrylonitrile composite nanofibers for a direct dye removal. *Fibers Polym.* **2015**, *16*, 1925−1934.
(25) Li, Z.-M.; Zhu, S.-X.; Mao, F.-F.; Zhou, Y.; Zhu, W.; Tao, D.-J. CTAB-controlled synthesis of phenolic resin-based nanofiber aerogels for highly efficient and reversible SO2 capture. *Chem. Eng. J.* **2022**, *431*, 133715.
(26) Liu, C.; Yin, Z.; Hu, D.; Mo, F.; Chu, R.; Zhu, L.; Hu, C. Biochar derived from chicken manure as a green adsorbent for naphthalene removal. *Environ. Sci. Pollut. Res. Int.* **2021**, *28*, 36585−36597.
(27) Zeng, H.; Qi, W.; Zhai, L.; Wang, F.; Zhang, J.; Li, D. Magnetic biochar synthesized with waterworks sludge and sewage sludge and its potential for methylene blue removal. *J. Environ. Chem. Eng.* **2021**, *9*, 105951.
(28) Yang, X.; Wang, L.; Shao, X.; Tong, J.; Chen, R.; Yang, Q.; Yang, X.; Li, G.; Zimmerman, A. R.; Gao, B. Preparation of biosorbent for the removal of organic dyes from aqueous solution via one-step alkaline ball milling of hickory wood. *Bioresour. Technol.* **2022**, *348*, 126831.
(29) Wu, J.; Yang, J.; Feng, P.; Huang, G.; Xu, C.; Lin, B. High-efficiency removal of dyes from wastewater by fully recycling litchi peel biochar. *Chemosphere* **2020**, *246*, 125734.
(30) Świechowski, K.; Matyjewicz, B.; Telega, P.; Białowiec, A. The Influence of Low-Temperature Food Waste Biochars on Anaerobic Digestion of Food Waste. *Materials* **2022**, *15*, 945.
(31) Xiao, J.; Xu, X.; Wang, F.; Ma, J.; Liao, M.; Shi, Y.; Fang, Q.; Cao, H. Analysis of exposure to pesticide residues from Traditional Chinese Medicine. *J. Hazard. Mater.* **2019**, *365*, 857−867.
(32) Hou, X.; Deng, Y.; Dai, M.; Jiang, X.; Li, S.; Fu, H.; Peng, C. Migration and transformation of heavy metals in Chinese medicine residues during the process of traditional pyrolysis and solar pyrolysis. *Chemosphere* **2022**, *293*, 133658.
(33) Lu, Q.; Li, C. Comprehensive utilization of Chinese medicine residues for industry and environment protection: Turning waste into treasure. *J. Cleaner Prod.* **2021**, *279*, 123856.
(34) Liu, R.; Yang, Z.; Wang, G.; Xian, J.; Li, T.; Pu, Y.; Jia, Y.; Zhou, W.; Cheng, Z.; Zhang, S.; Xiang, G.; Xu, X. Simultaneous removal of ammonium and phosphate in aqueous solution using Chinese herbal medicine residues: Mechanism and practical performance. *J. Cleaner Prod.* **2021**, *313*, 127945.
(35) Liu, X.; Zhou, Y.; Wang, C.-L.; Liu, Y.; Tao, D.-J. Solvent-free self-assembly synthesis of N-doped ordered mesoporous carbons as effective and bifunctional materials for CO_2 capture and oxygen reduction reaction. *Chem. Eng. J.* **2022**, *427*, 130878.
(36) Vigneshwaran, S.; Sirajudheen, P.; Karthikeyan, P.; Meenakshi, S. Fabrication of sulfur-doped biochar derived from tapioca peel waste with superior adsorption performance for the removal of Malachite green and Rhodamine B dyes. *Surf. Interfaces* **2021**, *23*, 100920.
(37) Liu, K. Effects of sample size, dry ashing temperature and duration on determination of ash content in algae and other biomass. *Algal Res.* **2019**, *40*, 101486.
(38) Lagergren, S. Zur theorie Der Sogenannten adsorption geloster stoffe, Kungliga Svenska Vetenskapsakademiens. *Handlingar* **1898**, *24*, 1−39.
(39) Ho, Y. S.; Wase, D. A. J.; Forster, C. F. Removal of lead ions from aqueous solution using sphagnum moss peat as absorbent. *Water SA* **1996**, *22*, 219−224.
(40) Weber, W. J.; Morris, J. C. Kinetics of adsorption on carbon from solution. *J. Sanit. Eng. Div., Am. Soc. Civ. Eng.* **1963**, *89*, 31.
(41) Langmuir, I. The adsorption of gases on plane surfaces of glass, mica and platinum. *J. Am. Chem. Soc.* **1918**, *40*, 1361−1403.
(42) Freundlich, H. M. F. Über die adsorption in lösungen. *Z. Physiol. Chem.* **1906**, *57*, 385−490.
(43) Sips, R. On the Structure of a Catalyst Surface. *J. Chem. Phys.* **1948**, *16*, 490−495.
(44) Wu, J.; Yang, J.; Huang, G.; Xu, C.; Lin, B. Hydrothermal carbonization synthesis of cassava slag biochar with excellent adsorption performance for Rhodamine B. *J. Cleaner Prod.* **2020**, *251*, 119717.
(45) Chen, X.; Ma, X.; Peng, X.; Lin, Y.; Yao, Z. Conversion of sweet potato waste to solid fuel via hydrothermal carbonization. *Bioresour. Technol.* **2018**, *249*, 900−907.
(46) Gao, L. Y.; Deng, J. H.; Huang, G. F.; Li, K.; Cai, K. Z.; Liu, Y.; Huang, F. Relative distribution of Cd2+ adsorption mechanisms on biochars derived from rice straw and sewage sludge. *Bioresour. Technol.* **2019**, *272*, 114−122.
(47) Patel, M.; Kumar, R.; Pittman, C. U., Jr.; Mohan, D. Ciprofloxacin and acetaminophen sorption onto banana peel biochars: Environmental and process parameter influences. *Environ. Res.* **2021**, *201*, 111218.
(48) Veiga, P.; Cerqueira, M. H.; Gonçalves, M. G.; Matos, T.; Pantano, G.; Schultz, J.; Andrade, J. B.; Mangrich, A. S. Upgrading from batch to continuous flow process for the pyrolysis of sugarcane bagasse: Structural characterization of the biochars produced. *J. Environ. Manage.* **2021**, *285*, 112145.
(49) Meng, X.; Hu, R. Nitrogen/phosphorus enriched biochar with enhanced porosity activated by guanidine phosphate for efficient passivation of Pb(II), Cu(II) and Cd(II). *J. Mol. Liq.* **2021**, *323*, 115071.
(50) Lee, L. Z.; Ahmad Zaini, M. A. One-step $ZnCl_2$/$FeCl_3$ composites preparation of magnetic activated carbon for effective adsorption of rhodamine B dye. *Toxin Rev.* **2020**, *41*, 64−81.
(51) Li, R.; Wang, Z.; Guo, J.; Li, Y.; Zhang, H.; Zhu, J.; Xie, X. Enhanced adsorption of ciprofloxacin by KOH modified biochar derived from potato stems and leaves. *Water Sci. Technol.* **2018**, *77*, 1127−1136.
(52) Gan, F.; Cheng, B.; Jin, Z.; Dai, Z.; Wang, B.; Yang, L.; Jiang, X. Hierarchical porous biochar from plant-based biomass through selectively removing lignin carbon from biochar for enhanced removal of toluene. *Chemosphere* **2021**, *279*, 130514.
(53) Salimi, P.; Javadian, S.; Norouzi, O.; Gharibi, H. Turning an environmental problem into an opportunity: potential use of biochar derived from a harmful marine biomass named *Cladophora glomerata* as anode electrode for Li-ion batteries. *Environ. Sci. Pollut. Res. Int.* **2017**, *24*, 27974−27984.
(54) Xiao, W.; Garba, Z. N.; Sun, S.; Lawan, I.; Wang, L.; Lin, M.; Yuan, Z. Preparation and evaluation of an effective activated carbon from white sugar for the adsorption of rhodamine B dye. *J. Cleaner Prod.* **2020**, *253*, 119989.
(55) Kord Mostafapour, F.; Zolghadr, R.; Khodadadi Saloot, M.; Mahvi, A. H.; Balarak, D.; Safari, E. Removal of Acid blue 113 from aqueous medium using a novel magnetic adsorbent derived from activated carbon fiber. *Int. J. Environ. Anal. Chem.* **2022**, 1−16.
(56) Asefi, D.; Arami, M.; Sarabi, A. A.; Mahmoodi, N. M. The chain length influence of cationic surfactant and role of nonionic co-surfactants on controlling the corrosion rate of steel in acidic media. *Corros. Sci.* **2009**, *51*, 1817−1821.
(57) Firoozi, M.; Rafiee, Z.; Dashtian, K. New MOF/COF Hybrid as a Robust Adsorbent for Simultaneous Removal of Auramine O and Rhodamine B Dyes. *ACS Omega* **2020**, *5*, 9420−9428.
(58) Du, X.-C.; Zhu, J.-H.; Quan, Z.-J.; Wang, X.-C. Adsorption of rhodamine B by organic porous materials rich in nitrogen, oxygen, and sulfur heteroatoms. *New J. Chem.* **2021**, *45*, 3448−3453.
(59) Huang, W.; Zhang, M.; Wang, Y.; Chen, J.; Zhang, J. Biochars prepared from rabbit manure for the adsorption of rhodamine B and

https://doi.org/10.1021/acsomega.2c06968
ACS Omega 2023, 8, 4813−4825

Congo red: characterisation, kinetics, isotherms and thermodynamic studies. *Water Sci. Technol.* **2020**, *81*, 436−444.
(60) Hou, Y.; Huang, G.; Li, J.; Yang, Q.; Huang, S.; Cai, J. Hydrothermal conversion of bamboo shoot shell to biochar: Preliminary studies of adsorption equilibrium and kinetics for rhodamine B removal. *J. Anal. Appl. Pyrolysis* **2019**, *143*, 104694.
(61) Albanio, I. I.; Muraro, P. C. L.; da Silva, W. L. Rhodamine B Dye Adsorption onto Biochar from Olive Biomass Waste. *Water, Air, Soil Pollut.* **2021**, *232*, 214.
(62) Li, R.; Wang, Z.; Zhao, X.; Li, X.; Xie, X. Magnetic biochar-based manganese oxide composite for enhanced fluoroquinolone antibiotic removal from water. *Environ. Sci. Pollut. Res.* **2018**, *25*, 31136−31148.
(63) Tan, W. T.; Zhou, H.; Tang, S. F.; Zeng, P.; Gu, J. F.; Liao, B. H. Enhancing Cd(II) adsorption on rice straw biochar by modification of iron and manganese oxides. *Environ. Pollut.* **2022**, *300*, 118899.
(64) Yorgun, S.; Yıldız, D. Preparation and characterization of activated carbons from Paulownia wood by chemical activation with H_3PO_4. *J. Taiwan Inst. Chem. Eng.* **2015**, *53*, 122−131.
(65) Xiang, Y.; Zhou, Y.; Yao, B.; Sun, Y.; Khan, E.; Li, W.; Zeng, G.; Yang, J.; Zhou, Y. Vinasse-based biochar magnetic composites: adsorptive removal of tetracycline in aqueous solutions. *Environ. Sci. Pollut. Res.* **2022**, DOI: 10.1007/s11356-022-19012-5.
(66) Liu, L.; Li, Y.; Fan, S. Preparation of KOH and H_3PO_4 Modified Biochar and Its Application in Methylene Blue Removal from Aqueous Solution. *Processes* **2019**, *7*, 891.
(67) Chen, M.; He, F.; Hu, D.; Bao, C.; Huang, Q. Broadened operating pH range for adsorption/reduction of aqueous Cr(VI) using biochar from directly treated jute (Corchorus capsularis L.) fibers by H3PO4. *Chem. Eng. J.* **2020**, *381*, 122739.
(68) Long, L.; Xue, Y.; Zeng, Y.; Yang, K.; Lin, C. Synthesis, characterization and mechanism analysis of modified crayfish shell biochar possessed ZnO nanoparticles to remove trichloroacetic acid. *J. Cleaner Prod.* **2017**, *166*, 1244−1252.
(69) Ge, Q.; Tian, Q.; Moeen, M.; Wang, S. Facile Synthesis of Cauliflower Leaves Biochar at Low Temperature in the Air Atmosphere for Cu(II) and Pb(II) Removal from Water. *Materials* **2020**, *13*, 3163.
(70) Huang, K.; Liu, F.; Fan, J. P.; Dai, S. Open and Hierarchical Carbon Framework with Ultralarge Pore Volume for Efficient Capture of Carbon Dioxide. *ACS Appl. Mater. Interfaces* **2018**, *10*, 36961−36968.
(71) Peng, H.-L.; Zhang, J.-B.; Zhang, J.-Y.; Zhong, F.-Y.; Wu, P.-K.; Huang, K.; Fan, J.-P.; Liu, F. Chitosan-derived mesoporous carbon with ultrahigh pore volume for amine impregnation and highly efficient CO_2 capture. *Chem. Eng. J.* **2019**, *359*, 1159−1165.

https://doi.org/10.1021/acsomega.2c06968
ACS Omega 2023, 8, 4813−4825